Check for updates

ADVANCED ENERGY MATERIALS
www.advenergymat.de

Reactive DC Sputtered TiO_2 Electron Transport Layers for Cadmium-Free Sb_2Se_3 Solar Cells

*Christopher H. Don, Thomas P. Shalvey, Daniya A. Sindi, Bradley Lewis, Jack E. N. Swallow, Leon Bowen, Daniel F. Fernandes, Tomas Kubart, Deepnarayan Biswas, Pardeep K. Thakur, Tien-Lin Lee, and Jonathan D. Major**

The evolution of Sb_2Se_3 heterojunction devices away from CdS electron transport layers (ETL) to wide bandgap metal oxide alternatives is a critical target in the development of this emerging photovoltaic material. Metal oxide ETL/Sb_2Se_3 device performance has historically been limited by relatively low fill factors, despite offering clear advantages with regards to photocurrent collection. In this study, TiO_2 ETLs are fabricated via direct current reactive sputtering and tested in complete Sb_2Se_3 devices. A strong correlation between TiO_2 ETL processing conditions and the Sb_2Se_3 solar cell device response under forward bias conditions is observed and optimized. Numerical device models support experimental evidence of a spike-like conduction band offset, which can be mediated, provided a sufficiently high conductivity and low interfacial defect density can be achieved in the TiO_2 ETL. Ultimately, a SnO_2:F/TiO_2/Sb_2Se_3/P3HT/Au device with the reactively sputtered TiO_2 ETL delivers an 8.12% power conversion efficiency (η), the highest TiO_2/Sb_2Se_3 device reported to-date. This is achieved by a substantial reduction in series resistance, driven by improved crystallinity of the reactively sputtered anatase-TiO_2 ETL, whilst maintaining almost maximum current collection for this device architecture.

1. Introduction

The development of thin-film photovoltaics (PV) has led to the commercialization of polycrystalline cadmium telluride (CdTe)-based devices which offer advantages over established silicon solar cells due to the less energy-intensive device fabrication and manufacturing processes. CdTe itself is not without its drawbacks; tellurium scarcity is often cited as a concern for widespread deployment, whilst the toxic heavy metal cadmium inclusion raises questions about end-of-life environmental implications. Thus, it is necessary to explore alternative materials suitable for fulfilling the wide range of evolving PV applications (building integrated (BIPV), tandem top and bottom cell etc.).

Inorganic chalcogenides are another class of materials being studied–many with qualities that make them versatile options for PV. Most notably, $CuIn_{1-x}Ga_xSe_2$ (CIGS) and kesterite $Cu_2ZnSn(S,Se)_4$ materials (CZTS), have drawn significant scientific interest. Whilst CIGS has achieved an impressive 23.6% power conversion efficiency (η),[1] the elemental abundance issue remains unsolved with the inclusion of In/Ga, and the requirement for Cd, while reduced, is still present in cadmium sulfide (CdS) as the electron transport layer (ETL). Despite its CdS ETL, CZTS utilizes an entirely

C. H. Don, T. P. Shalvey, D. A. Sindi, B. Lewis, J. D. Major
Stephenson Institute for Renewable Energy
Department of Physics
University of Liverpool
Liverpool L69 7ZF, UK
E-mail: jonmajor@liverpool.ac.uk

D. A. Sindi
Department of Physics
College of Science
Umm Al-Qura University
Makkah 24382, Saudi Arabia

The ORCID identification number(s) for the author(s) of this article can be found under https://doi.org/10.1002/aenm.202401077

© 2024 The Author(s). Advanced Energy Materials published by Wiley-VCH GmbH. This is an open access article under the terms of the Creative Commons Attribution License, which permits use, distribution and reproduction in any medium, provided the original work is properly cited.

DOI: 10.1002/aenm.202401077

J. E. N. Swallow
Department of Materials
University of Oxford
Parks Road, Oxford OX1 3PH, UK

L. Bowen
Department of Physics
University of Durham
Durham DH1 3LE, UK

D. F. Fernandes, T. Kubart
Department of Electrical Engineering
Division of Solid-State Electronics
The Ångström Laboratory
Uppsala University
SE-751 03 Uppsala, Sweden

D. Biswas, P. K. Thakur, T.-L. Lee
Diamond Light Source Ltd, Diamond House
Harwell Science and Innovation Campus
Didcot, Oxfordshire OX11 0DE, UK

16146840, 0, Downloaded from https://onlinelibrary.wiley.com/doi/10.1002/aenm.202401077 by Test, Wiley Online Library on [18/06/2024]. See the Terms and Conditions (https://onlinelibrary.wiley.com/terms-and-conditions) on Wiley Online Library for rules of use; OA articles are governed by the applicable Creative Commons License

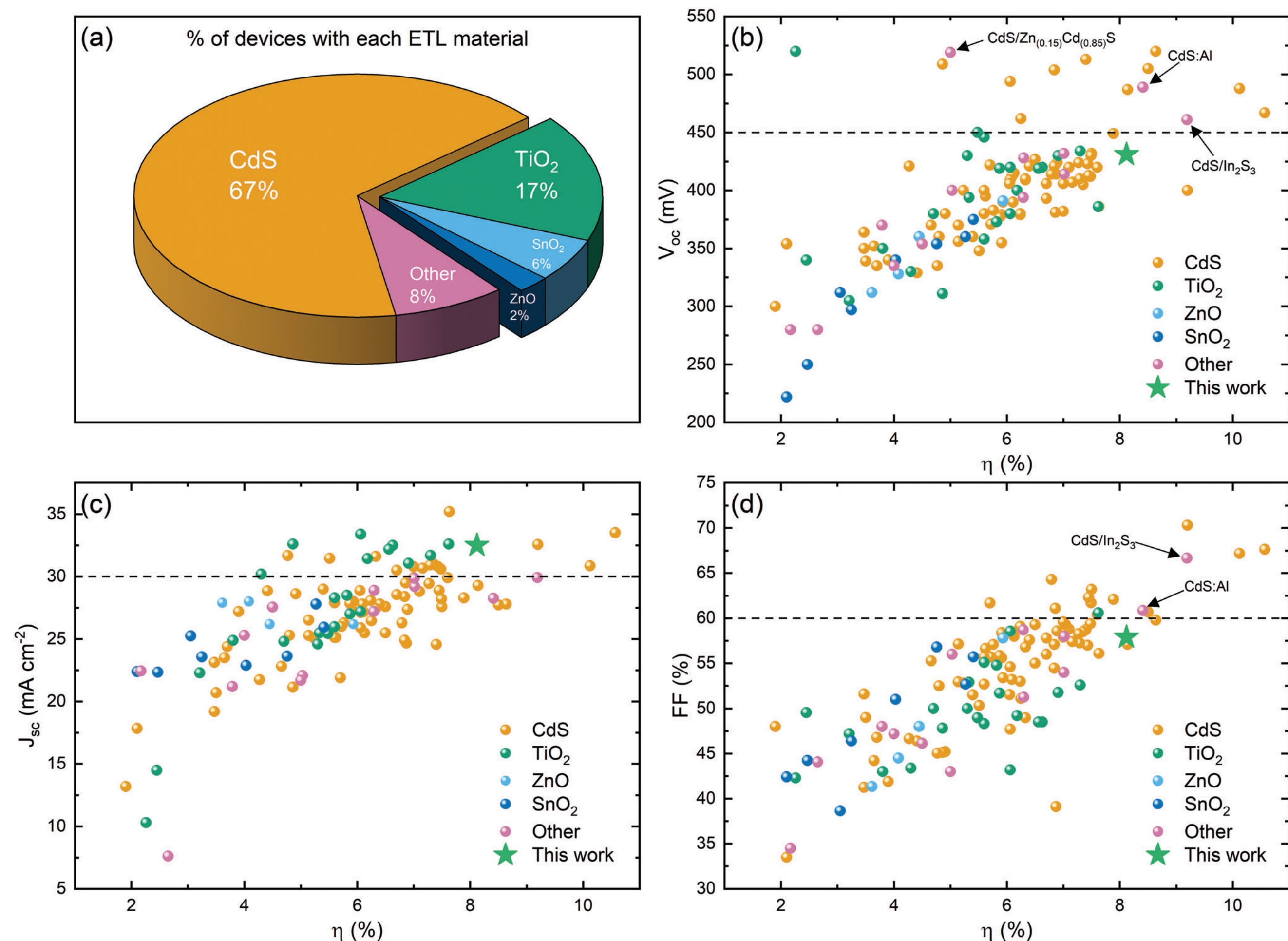

Figure 1. a) Percentage of $Sb_2(S,Se)_3$ devices with each ETL (N = 171). Sb_2Se_3 Device performance results for b) V_{oc}, c) J_{sc}, and d) FF as a function of η found in the literature for various ETLs. Reproduced and updated with permission.[13]

earth-abundant device structure to achieve 13.6% η, however, industrial scalability is in question due to the common formation of unwanted secondary phases during material synthesis.[2]

Both antimony selenide (Sb_2Se_3) and antimony sulfide (Sb_2S_3) are thin-film PV absorber materials currently gathering momentum. With respective optical bandgaps of 1.2 and 1.7 eV,[3,4] they offer versatility as both top and bottom cells for tandem devices, but also single-junction capability in the form of the sulfoselenide ($Sb_2(S,Se)_3$) alloy system which allows for bandgap tunability due to the shared 1D "nanoribbon" crystal structure.

In addition to its favorable optoelectronic properties, $Sb_2(S,Se)_3$ offers earth abundance, low toxicity and high stability.[5–7] Rapid increases in device performance have progressed efficiency records to 10.57% and 10.75% for Sb_2Se_3 and $Sb_2(S,Se)_3$, respectively.[8,9]

A recent life-cycle analysis (LCA) by Resalati et al. has shown that provided efficiencies equivalent to CIGS can be obtained, there would be an environmental benefit of Sb_2Se_3.[10] The study assumed that all devices were in a substrate architecture with a CdS ETL. Thus, eradicating the requirement for Cd completely in the device structure, would offer further advantage to this emerging material. The eventual transition from CdS to metal oxide ETLs ($Mg_{1-x}Zn_xO$ and SnO_2) during CdTe development was an important step for commercialization.[11–13] Undeniably the same must also happen for $Sb_2(S,Se)_3$, not only from an LCA standpoint but also in terms of attainable quantum efficiency due to the parasitic absorption of blue light by the 2.4 eV CdS bandgap and resulting transmission loss to the photoactive layer.[14–16]

Figure 1a distinguishes the ETL of devices reported across $Sb_2(S,Se)_3$ literature. Pure CdS is evidently the most common, making up two-thirds of devices and often integrated into the more complex structures designated to the "other" category. It is surprising that the combined representation of metal oxides is limited to just 25% of devices, given that the breakthrough $Sb_2(S,Se)_3$ solar cell work began as an offshoot of dye-sensitized solar cells (DSSC) which incorporated some combination of both planar and mesoporous titanium dioxide (TiO_2) at the junction interface.[17–20]

Since drawing open-circuit voltage (V_{oc}) and short-circuit current density (J_{sc}) comparisons for devices across the alloy composition is futile, only Sb_2Se_3 devices from the literature are included in Figure 1b–d (N = 135). Looking first at the V_{oc} of these devices as a function of η (Figure 1b), it can be seen that the only devices consistently exceeding 450 mV are those with a CdS

© 2024 The Author(s). Advanced Energy Materials published by Wiley-VCH GmbH

junction, with the exception of a 520 mV TiO_2 outlier in an early study by Zhou et al.[18] The next highest V_{oc} reported with TiO_2 is just below 450 mV, although it would appear that these studies did not include any method to remedy selenium deficiency in the Sb_2Se_3 films which is commonly cited as a source of V_{oc} loss.[21–25] It is also worth noting that of the 14 reported devices >450 mV, ten of those were in a substrate device geometry with a Mo hole contact, which may partially explain the relative success of CdS with regards to V_{oc}.

The performance limiting inter-diffusion at the CdS/Sb_2Se_3 interface, observed for devices of both substrate and superstrate geometries, is well-established.[24,26–28] In the case of superstrate devices, this introduces constraints on possible high-temperature post-deposition selenization treatments of the absorber which would damage the CdS/Sb_2Se_3 interface. The high stability of the TiO_2/Sb_2Se_3 interface during high-temperature exposure is a significant benefit in this regard (Figure S1, Supporting Information).[29]

As expected, wide bandgap TiO_2 ETL Sb_2Se_3 devices outperform CdS, in terms of J_{sc} (Figure 1c), due to the parasitic absorption from the narrow 2.4 eV CdS bandgap heavily studied and optimized in CdTe literature which limits the collection from the blue part of the spectrum. The exception here is a reported 35 mA cm^{-2} CdS partner device from Dong et al. which appears to be a record for Sb_2Se_3, although external quantum efficiency (EQE) measurements are absent.[25]

Whilst the V_{oc} advantage in CdS ETL Sb_2Se_3 devices over TiO_2 may be explained by substrate geometry and selenization efforts, the fill factor (*FF)* of the best CdS ETL devices (≈70%) is still above that of TiO_2 (≈60%)(Figure 1d). These parameters are of course intrinsically linked through non-radiative recombination, however, low Sb_2Se_3 device *FF*s cannot be explained purely by V_{oc}-deficit as illustrated by the 400 mV V_{oc} device by Li et al. with >70% *FF*.[27] Clearly, there is still significant room for the development of Sb_2Se_3 device architectures to improve selective carrier transport, which appears to be a bigger issue, at present, for metal oxide ETL devices (Figure 1).

The widely implemented organic hole transport layers (HTL) (Spiro-OMeTAD, P3HT etc.) in superstrate devices offer a two-birds-one-stone solution to both low shunt resistance (R_{sh}) and forward-bias rollover caused by the Sb_2Se_3/Au interface.[7] This is achieved by simultaneously pinhole blocking shunt pathways and improving charge selectivity at the hole contact to improve both average and peak cell *FF*s.

For electron transport, there are two studies outside of our group which report on TiO_2 processing optimization in $Sb_2(S,Se)_3$ literature. The first study by Chen et al. varied post-deposition anneal temperatures of their spray-pyrolysis deposited TiO_2 and concluded that reduced deep-level defects in the 450 °C sample resulted in improved Sb_2Se_3 solar cell performance.[30] Koltsov et al. compared the effects of vacuum and air annealing of their spray-pyrolysis TiO_2 and suggested that an initial low-temperature vacuum anneal, prior to the typical 450 °C air anneal, improved performance by reducing organic residues in resulting films.[31] Both studies omit current density–voltage (*J*–*V*) curves for these sections, but a significant *FF* dependence is observed in reported *J*–*V* parameters (as low as ≈30% which is approaching a flat line in the power quadrant), suggesting severe "S-shape" *J*–*V* distortion.

Previously, we have reported on *FF* limiting *J*–*V* distortion which is induced by charge barriers from defective TiO_2 ETLs.[32] They appear influenced by poor crystallinity, defect-driven photoconductivity and mixed-phase films of this polymorphic material. In the aforementioned study, Sb_2Se_3 solar cells with radio frequency (RF) magnetron sputtered TiO_2 ETLs were deposited from a compound TiO_2 target, although optimization efforts in this case were limited by reproducibility issues. The stubborn adherence to CdS ETLs, rather than TiO_2, may be due to the relative difficulty of producing monophasic TiO_2 with reliable electronic properties, compared to CdS.

For charge separation and selective carrier transport in solar cells, there must be an asymmetry in the electron and hole conductivities.[33–35] In p-i-n heterojunction devices, the functionality of the ETL and HTL is critical to achieve this.[33] For efficient selectivity, the ETL/absorber interface is required to have a minimal conduction band offset (*CBO*) and a large valence band offset (*VBO*) to facilitate electron transport whilst impeding hole transport. It is well established that a type-I ("spike") *CBO* can lead to *J*–*V* distortion from the resulting interfacial charge barrier for electrons and a subsequent collapse in device *FF*.[36–40]

Band position measurements via photoemission spectroscopy for both TiO_2 and Sb_2Se_3 are numerous and hugely variant.[32,41–45] Figure S2 (Supporting Information) shows two examples in the literature which report a –0.50 eV *CBO* "cliff" and a +0.71 eV *CBO* spike (a relative *CBO* difference of 1.21 eV).[42,43] This variance of band positions for what is an intrinsic material property is of course unphysical and highlights limitations in the band alignment method. Determination of the ionization potential via photoemission introduces measurement uncertainties; spectrometer calibration, charging, linear extrapolation of both the valence band maximum (*VBM*) and secondary electron cutoff (*SEC*), and caveats; surface sensitivity, alignment of Fermi levels, band bending upon interface formation, interface defect pinning. For photoactive materials and multi-layer stacks, there are additional effects from both junction and surface photovoltages which can be induced by stray light, or even the measurement beam itself.[46] To obtain the conduction band minima (*CBM*) from the ionization potential, the fundamental energy gap (E_g) must be subtracted, the measurement of which is itself non-trivial.[47] A study by Shiel et al. compared the TiO_2/Sb_2Se_3 *CBO* positions obtained with three different band alignment methods and reported *CBO* values ranging from a +0.11 eV spike to a –0.82 eV cliff.[41]

Given that *J*–*V* distortion from devices with TiO_2/Sb_2Se_3 interfaces appears to be a universal problem,[30–32] this may be the best evidence for a *CBO* spike of these materials after interface formation. These previous reports, along with the present study, suggest the barrier to electron transport can be mediated by optimized TiO_2 processing, provided sufficiently high electron conductivities and low interfacial defect densities can be obtained.

In this study, we report a simple, scalable, reproducible method of preparing highly crystalline wide bandgap anatase-TiO_2 thin films for application as the ETL in Sb_2Se_3 solar cells. An SnO_2:F/TiO_2/Sb_2Se_3/P3HT/Au device fabricated with a reactively sputtered TiO_2 ETL achieved an improved 8.12% η due to significantly reduced series resistance (R_s) compared to similar device structures. Differences in the TiO_2 films obtained from both precursor solution and sputtering are compared and

© 2024 The Author(s). Advanced Energy Materials published by Wiley-VCH GmbH
16146840, 0, Downloaded from https://onlinelibrary.wiley.com/doi/10.1002/aenm.202401077 by Test, Wiley Online Library on [18/06/2024]. See the Terms and Conditions (https://onlinelibrary.wiley.com/terms-and-conditions) on Wiley Online Library for rules of use; OA articles are governed by the applicable Creative Commons License

16146840, 0, Downloaded from https://onlinelibrary.wiley.com/doi/10.1002/aenm.202401077 by Test, Wiley Online Library on [18/06/2024]. See the Terms and Conditions (https://onlinelibrary.wiley.com/terms-and-conditions) on Wiley Online Library for rules of use; OA articles are governed by the applicable Creative Commons License

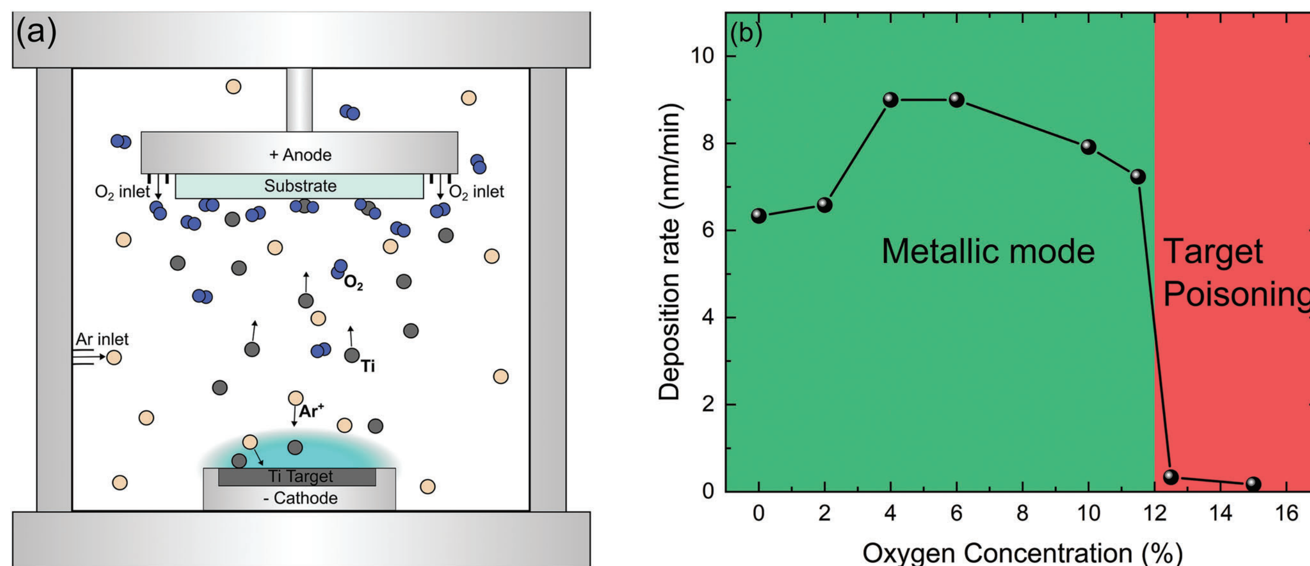

Figure 2. a) Illustration of the reactive sputtering process. b) Film deposition rate from a Ti sputtering target as a function of oxygen flow concentration ($[O_2/(O_2 + Ar)] \times 100$) at 5 mTorr pressure and 5 W cm^{-2} DC power density.

discussed in the context of *FF* variance in completed TiO_2/Sb_2Se_3 devices. The results are supported by numerical simulations which detail the device's physics and serve as a guide to future device processing where additional gains can be made.

2. Results and Discussion

2.1. Reactive Sputtering of TiO_2 Thin-Films

Magnetron sputter deposition techniques present an opportunity for scalable physical vapor deposition (PVD) of a wide range of materials, irrespective of their melting point. This is of particular importance for materials with low vapor pressure, such as the ETLs explored in Sb_2Se_3 heterojunction solar cell device literature (CdS, TiO_2, SnO_2, ZnO). In the case of sputtering from compound ("ceramic") targets of these materials, RF sputtering is frequently needed due to the insulating nature of the sputtering targets. RF sputtering, however, requires more complex hardware and achieves lower deposition rates for the same discharge power as compared to DC sputtering. It is therefore advantageous to use reactive magnetron sputtering from a metallic target by introduction of a reactive gas such as O_2/N_2, in addition to the working gas (Ar), to deliver compound films with a high deposition rate via DC sputtering.[48,49]

A major consideration during DC reactive sputtering is that the amount of reactive gas introduced has to be carefully controlled in order to avoid target poisoning. For the case of reactive sputter deposition of titanium oxide films from a Ti target, at high O_2/Ar partial pressures, when the rate of target oxidation from the reactive O_2 gas exceeds the rate that those species are re-sputtered back off the surface, then the Ti sputter yield decreases as a result of the surface oxidation.[50] This further accelerates the target oxidation, and a runaway effect essentially reduces the deposition rate to a fraction of that achieved at lower O_2/Ar partial pressures. This process exhibits a hysteresis effect whereby the O_2 flow rate must be significantly reduced below the partial pressure which induces target poisoning to return it to the metallic state.[51] The two regions with very different deposition rates are shown in **Figure 2**b. Although a high deposition rate can be achieved in the metallic mode, the deposited film is typically oxygen deficient.

The customary approach to preparing anatase-TiO_2 is to initially fabricate an amorphous film at a low temperature (<150 °C), and subsequently sinter in air at ≈450 °C which recrystallizes the amorphous TiO_2 toward anatase-TiO_2.[52,53] Thus, initial titanium oxide films were deposited at room temperature (RT). To test the dependence of reactive oxygen incorporation on deposition rate, films were independently sputtered from a Ti target for 60 min at constant $O_2/(O_2+Ar)$ flow rate, with a 5 min "pre sputter" in 100% Ar between runs to clean the target surface of residual oxygen and reset any hysteresis conditioning. It can clearly be seen from Figure 2 that target poisoning occurs between 11.5% and 12.5% O_2 flow rate, although the deposition rate starts to significantly reduce already by 10.0% O_2.

As-deposited titanium oxide films sputtered in the metallic mode (<10.0% O_2) suffer from sub-stoichiometry (<2:1 O:Ti), indicated by a visible grey darkening of the film and subsequent reduction in spectral transmission. For the case of RT reactively sputtered films, this is easily remedied by a low temperature post-deposition air anneal at 200 °C for 60 min—well below the typical sintering temperatures employed to form anatase phase TiO_2 (Figure S3, Supporting Information). This is not the case for metallic Ti films (0% O_2) for which the transmission is reduced even for an increased 550 °C post-deposition air anneal (Figure S4, Supporting Information), or for the case where the substrate is heated during sputter deposition, as discussed later.

Whilst the effects of other sputtering parameters can be explored (target power density, deposition pressure), oxygen utilization and subsequent plasma properties will be affected, thus the target poisoning regime in Figure 2b would need to be calibrated for each case. For this study, a high power density (5 W cm^{-2}) and low pressure (5 mTorr) were fixed to deliver a high

© 2024 The Author(s). Advanced Energy Materials published by Wiley-VCH GmbH

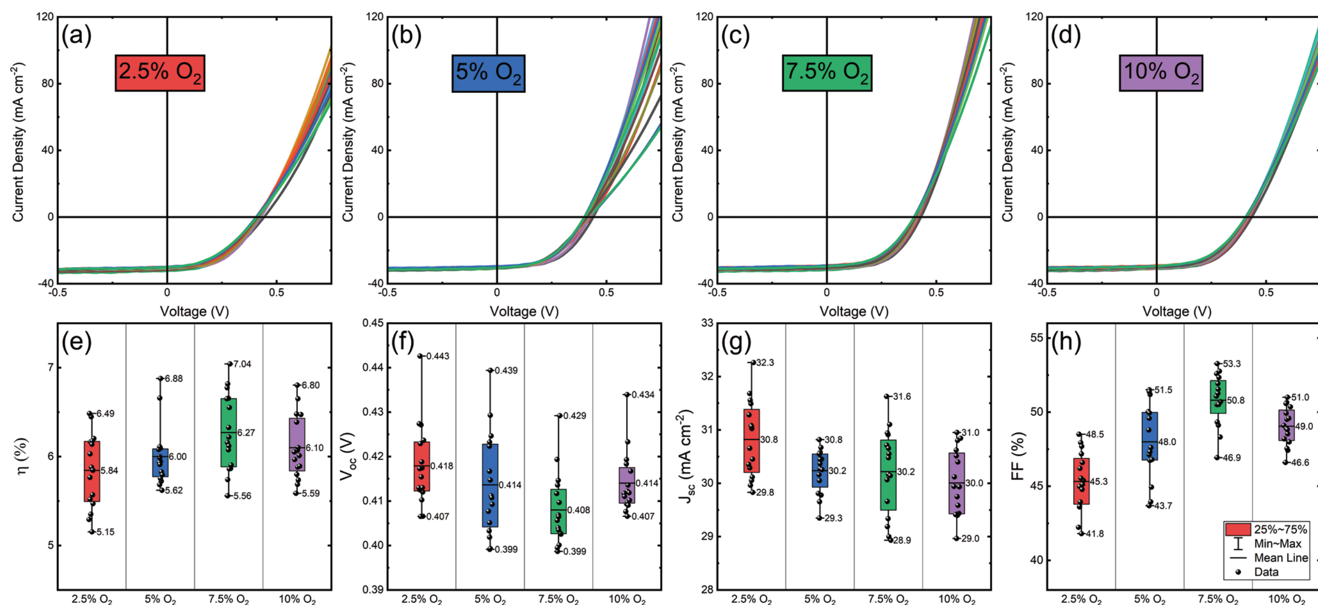

Figure 3. J–V curves at AM1.5 for Sb_2Se_3 devices (N=16) with reactively sputtered TiO_2 ETLs sputtered at a) 2.5%, b) 5.0%, c) 7.5%, and (d) 10.0% O_2 flow rate. Box and whisker plots for extracted J–V parameters e) η, f) V_{oc}, g) J_{sc}, and h) FF.

deposition rate, suitable for industrial scalability. Dedicated TiO_2 sputtering literature exploring additional parameter space can be found elsewhere.[49,54,55]

2.2. Device Optimization

After establishing the operating range of reactive O_2 flow rate during deposition, complete Sb_2Se_3 devices were fabricated as outlined in the experimental section with TiO_2 ETLs of varying O_2 flow rate (2.5%, 5.0%, 7.5%, and 10.0%) deposited at RT and post-annealed at 450 °C in the air for 60 min. The TiO_2 film thicknesses for 2.5%, 5.0%, 7.5% and 10.0% were measured as 107, 101, 99, and 70 nm respectively.

The device performance results from **Figure 3** show that the η dependence correlates primarily with FF. This is driven by improvements in the forward bias regime as seen in Figure 3a–d and reduction in R_s with increasing O_2 flow rate from 2.5% to 7.5% (Figure S5, Supporting Information). Whilst the 10.0% O_2 devices don't follow the same trend, we attribute that to the thinner TiO_2 film in this sample which introduces "S-shape" J–V distortion as will be shown next. As the O_2 flow rate approaches the target poisoning domain (i.e., $\geqslant$10.0%), process instability is introduced which limits control of deposition rate and consequent sample reproducibility. Thus, 7.5% O_2 was selected for further optimization efforts and all subsequent devices presented in this study. However, we consider that operating as close to the target poisoning regime as possible may be beneficial, provided stability is maintained via feedback control systems and plasma emission monitoring.[56]

Upon identification of suitable sputtering conditions to provide reproducible TiO_2 films with high deposition rate and optical transparency, the ETL film thickness was varied to understand the impact on the Sb_2Se_3 device performance. The device η results in **Figure 4** again show a strong correlation with FF, although seemingly through a different mechanism. In this case the introduction of a barrier to charge extraction, indicated by the S-shape J–V distortion in both the 25 and 60 nm (Figure 4a,b) TiO_2 devices, drastically reduces FF.[39,40] Meanwhile for the device with a 330 nm TiO_2 ETL, the parasitic resistance contribution to R_s is increased and current loss is evident in reverse bias, likely due to a reduction in transmission through the thicker window layer. X-ray diffraction (XRD) of the Sb_2Se_3 films which produced the devices in Figure 4 all show a nominal (primarily (211) and (221)) film orientation, free of hk0 flat-lying grains (Figure S6, Supporting Information).

In CdTe literature, device V_{oc} falls considerably when the CdS ETL thickness is reduced below 100 nm.[11] Such an effect is not observed here for the case of the TiO_2/Sb_2Se_3 junction where V_{oc} appears independent of ETL thickness. The study by Kephart et al. concludes that poor band alignment is the cause of V_{oc} loss. This is further supported by a V_{oc} improvement after the addition of low electron affinity (χ_e) transport layers which eliminate the cliff-like CBO.[11] The distinction between these two opposing behaviors is characteristic of cliff-like and spike-like CBOs for the CdS/CdTe and TiO_2/Sb_2Se_3 interfaces, respectively.

During the transition to metal oxide ETLs, CdTe devices similarly struggled with charge accumulation at the ETL/absorber interface and resulting J–V distortion,[11,57–62] which was eventually alleviated through interface engineering with $CdSe_xTe_{1-x}$ (CST) absorber grading at the junction. The current record $TiO_2/Sb_2(S,Se)_3$ device similarly benefited from absorber grading with a sulfur-rich junction to suppress interfacial carrier recombination.[63]

Besides our previous report which details J–V distortion in devices caused by the TiO_2/Sb_2Se_3 interface,[32] to our knowledge, no other such report exists despite indicators in the FF

© 2024 The Author(s). Advanced Energy Materials published by Wiley-VCH GmbH

16146840, 0, Downloaded from https://onlinelibrary.wiley.com/doi/10.1002/aenm.202401077 by Test, Wiley Online Library on [18/06/2024]. See the Terms and Conditions (https://onlinelibrary.wiley.com/terms-and-conditions) on Wiley Online Library for rules of use; OA articles are governed by the applicable Creative Commons License

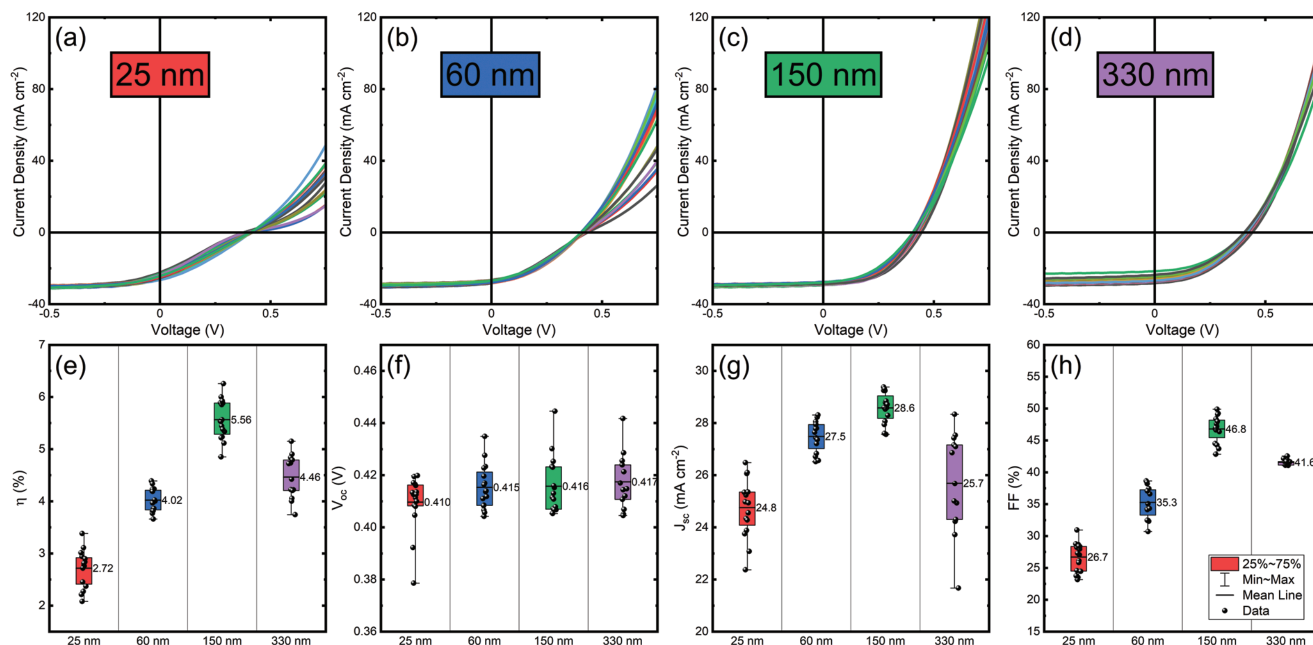

Figure 4. *J–V* curves at AM1.5 for Sb_2Se_3 devices (N=16) with reactively sputtered TiO_2 ETLs of a) 25 nm, b) 60 nm, c) 150 nm, and d) 330 nm thickness. Box and whisker plots for extracted *J–V* parameters e) η, f) V_{oc}, g) J_{sc}, and h) *FF*.

dependencies.[30,31] Whether this is due to relatively few groups working on TiO_2 ETL devices or a symptom of groups opting not to report unsuccessful fabrication efforts remains to be seen. Frequent reporting of device *J–V* measurements limited to only the "power" quadrant is another factor in obscuring performance-limiting characteristics observable under both reverse and forward bias conditions.

Regardless, for optimization purposes, additional devices were fabricated with a more refined thickness range (100–150 nm) due to the high *FF* observed for the 99 and 150 nm devices in Figures 3c and 4c. The device results can be found in Figure S7 (Supporting Information), however, no obvious performance trend was observed. Clearly, any marginal gains to be had in this range are currently obscured by larger variances in the full device fabrication process.

2.3. TiO_2 Film Characterization

In previous attempts to fabricate TiO_2 ETLs via magnetron sputtering from a compound target, poor crystallinity and lack of phase control in the attained films were a significant issue.[32] Those films were similarly sputtered at RT, with a high-temperature post-deposition air anneal, typical of those widely reported in the literature to form polycrystalline anatase phase TiO_2 from chemical precursors. The previous compound sputtered and post-annealed films were amorphous in nature when examined via X-ray diffraction, with a mix of both rutile and anatase signatures identified through bulk Raman and surface X-ray photoemission spectroscopy (XPS) measurements.[32] Where strong diffraction is not observed, Raman spectroscopy is a complementary method of characterizing bulk material phase. Due to the nature of the measurement which is sensitive to characteristic vibrational modes, long-range lattice order is not a prerequisite for phase detection.

To assess the titanium oxide phase attained in films reactively sputtered with 7.5% O_2, Raman spectra were recorded from RT deposited films with increasing post-deposition air anneal temperatures (**Figure 5a**). Spectra obtained from solution spin-coated TiO_2 films from titanium isopropoxide (TTIP) precursor with an anneal process in the same range are shown in Figure 5b for reference. The emergence of characteristic vibrational modes for anatase-TiO_2 at 280 °C in the reactively sputtered films is significantly lower temperature than is needed to recrystallize the solution spin-coated amorphous films, which show no anatase signal below 375 °C.[64,65] The anatase signal intensity continues to increase with temperature up to 450 °C anneal typically employed in literature, and additionally used to produce the SnO_2:F/TiO_2/Sb_2Se_3/P3HT/Au devices in Figures 3 and 4.

For superstrate PVD-grown absorber devices, a lower ETL anneal temperature is needless, since the substrate temperature during the close-space sublimation (CSS) process can be as high as 490 °C at present. This result of low-temperature anatase-TiO_2 formation does, however, open up the possibility of incorporation into more temperature-sensitive device architectures such as substrate geometry devices and those with flexible polymer substrates or AZO/ITO transparent front contacts.

Core level (CL) XPS at two different photon energies was employed on the reactively sputtered titanium oxide films with various post-deposition anneal temperatures to expose chemical and compositional information. By operating at both soft (1090 eV) and hard (5925 eV) photon energies, relative surface and more bulk-appropriate effects can be discerned.[41]

Figure 6a,b shows XPS and hard X-ray photoelectron spectroscopy (HAXPES) Ti 2p spectra, respectively, of the titanium oxide film with four anneal conditions overlayed. It can be seen

© 2024 The Author(s). Advanced Energy Materials published by Wiley-VCH GmbH

16146840, 0, Downloaded from https://onlinelibrary.wiley.com/doi/10.1002/aenm.202401077 by Test, Wiley Online Library on [18/06/2024]. See the Terms and Conditions (https://onlinelibrary.wiley.com/terms-and-conditions) on Wiley Online Library for rules of use; OA articles are governed by the applicable Creative Commons License

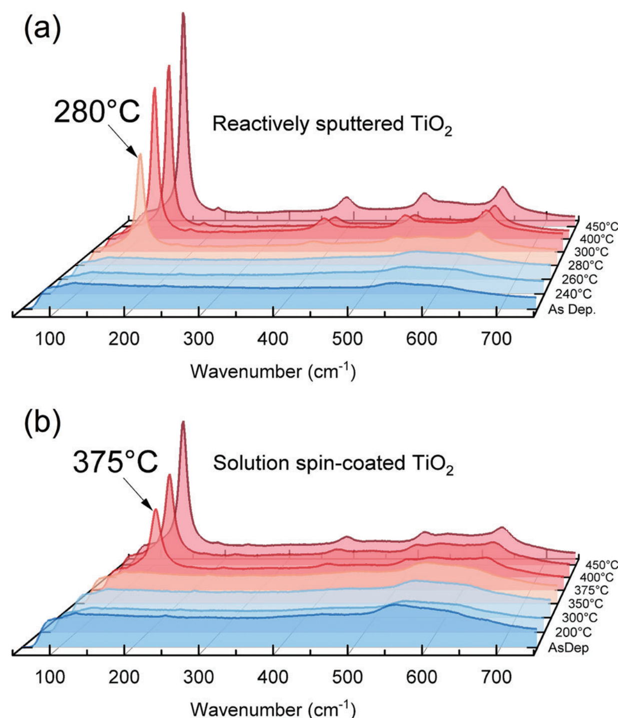

Figure 5. Raman spectra of RT a) reactively sputtered and b) solution spin-coated TiO_2 thin-films deposited on SnO_2:F with various post-deposition air anneal temperatures.

that the titanium is primarily in the assigned 4+ oxidation state associated with TiO_2, in agreement with the anatase-TiO_2 Raman signal seen in films annealed at >280 °C in Figure 5. It can also be seen that most obviously in the as-deposited film but also diminishing with anneal temperature, a low binding energy (BE) shoulder is present. This is widely reported in the literature to belong to Ti^{3+}(Ti_2O_3), rather than Ti^{2+}(TiO) or metallic Ti which would be expected to feature at much lower BE (–3.3 and –4.8 eV, respectively), relative to Ti^{4+}(TiO_2).[66,67] It should be noted that formal oxidation state assignment here is based purely on those assigned for titanium oxides in XPS literature, however in reality the true chemical bonding mechanisms are more complex.[68,69]

By comparing the soft (Figure 6a) and hard X-ray spectra (Figure 6b), it can be seen that the Ti_2O_3 feature increases in the as-deposited film for the hard photon energy compared to the soft as we probe deeper into the material. Whilst air exposure was limited to ≈3 h between film deposition and UHV loading, this suggests some natural oxidation of the surface toward more stoichiometric TiO_2, relative to the bulk. This surface and bulk comparison also provide good evidence that although sub-stoichiometric TiO_2 was deposited via the reactive sputtering method, the post-deposition air anneal treatment is oxidizing subsurface titanium toward 2:1 O/Ti TiO_2. According to the phase diagram from Samsonov,[70] later reproduced by Diebold,[71] Ti_2O_3 is the dominant phase for $1.2 < O/Ti < 1.6$, although the oxygen content in as-deposited films reactively sputtered at 7.5% O_2 is likely much higher than this based on the significant Ti^{4+}(TiO_2) photoemission signal. Extinction of the Ti^{3+} HAXPES feature is the best evidence for achieving 2:1 stoichiometry at least beyond the resolution of alternative methods of composition determination such as energy dispersive X-ray spectroscopy (EDX).

Another feature of the spectra is the shift to higher BE of the Ti^{4+} $2p_{3/2}$ CL with increased anneal temperature. Since the CL→valence band (*VB*) energy distance is considered a material constant, this suggests the *VB*→Fermi level (E_F) is increasing, i.e., the material is becoming more n-type. Full peak fitted spectra (Figures S8 and S9, Supporting Information), extracted peak positions and widths (Tables S1 and S2, Supporting Information), along with information regarding fitting constraints applied can be found in the supplemental information.

Grazing incidence X-ray diffractograms (GIXRD) in **Figure 7** confirm highly crystalline anatase-TiO_2 is formed via the reactive sputtering and post-deposition air anneal method due to the intense, narrow diffraction peaks which agree well with the anatase PDF card (9008216), although shifted to a higher 2θ angle relative to the simulated powder reference. This effect is due to refraction of the X-ray beam which occurs for incident angles approaching the critical angle.[76] The anatase-TiO_2 peak intensity increases considerably in the 450 °C annealed film relative to the 280 °C, indicating some crystallinity improvement in the anatase-TiO_2 between this temperature range. No additional signal from rutile-TiO_2 is observed at 450 °C demonstrating that the annealing treatment is below the threshold for anatase-rutile conversion, in this case, reported to occur between 400–1200 °C dependent on the crystalline quality of the anatase.[64] The peak widths observed here for reactively sputtered-TiO_2 films are far narrower than is attained via fabrication of TTIP solution spin-coated TiO_2 films with equivalent post-deposition anneal conditions (Figure S10, Supporting Information). An additional peak is observed at 24.2° due to radiation contamination of W filament on the Cu anode. Calculated anatase-TiO_2 spectra from a W Lα source are included in Figure S10 (Supporting Information).

Scanning electron microscopy (SEM) images of the reactively sputtered TiO_2 films—both as-deposited and post-annealed—show no apparent morphological reconstruction of the large 100 nm agglomerations despite significant changes in Raman, XPS and GIXRD (**Figure 8**). It is possible that the grainy texture within the agglomerations is softening and becoming more rounded with the post-deposition air anneal treatment. A high-resolution transmission electron microscopy (HRTEM) image of the final TiO_2 film, taken from a device cross-section, is shown in Figure 8d. Both the electron contact (SnO_2:F) (red) and absorber (Sb_2Se_3) (green) interfaces with the TiO_2 ETL can be observed in the bottom-left and top-right of the image, respectively. The high level of crystallinity achieved via the reactive sputtering method is evident throughout the bulk and also in the near-interface regions. This is not the case for TiO_2 fabricated via the solution spin-coated method, which shows little diffraction (Figure S11, Supporting Information). No inter-diffusion is observed at the TiO_2/Sb_2Se_3 interface. Crystalline Sb_2Se_3 ribbons demonstrate favorable adhesion to the TiO_2 despite its roughness which results from the conformal sputtered coating of the SnO_2:F.[32] This level of ETL material and interface quality is necessary from a device perspective to achieve electron selectivity. The large Sb_2Se_3 grain structure obtained via CSS growth on the sputtered TiO_2 is shown in Figure 8e.

Depositing TiO_2 films at increased substrate temperature was explored. These films were post-annealed as standard, however,

© 2024 The Author(s). Advanced Energy Materials published by Wiley-VCH GmbH

16146840, 0, Downloaded from https://onlinelibrary.wiley.com/doi/10.1002/aenm.202401077 by Test, Wiley Online Library on [18/06/2024]. See the Terms and Conditions (https://onlinelibrary.wiley.com/terms-and-conditions) on Wiley Online Library for rules of use; OA articles are governed by the applicable Creative Commons License

16146840, 0, Downloaded from https://onlinelibrary.wiley.com/doi/10.1002/aenm.202401077 by Test, Wiley Online Library on [18/06/2024]. See the Terms and Conditions (https://onlinelibrary.wiley.com/terms-and-conditions) on Wiley Online Library for rules of use; OA articles are governed by the applicable Creative Commons License

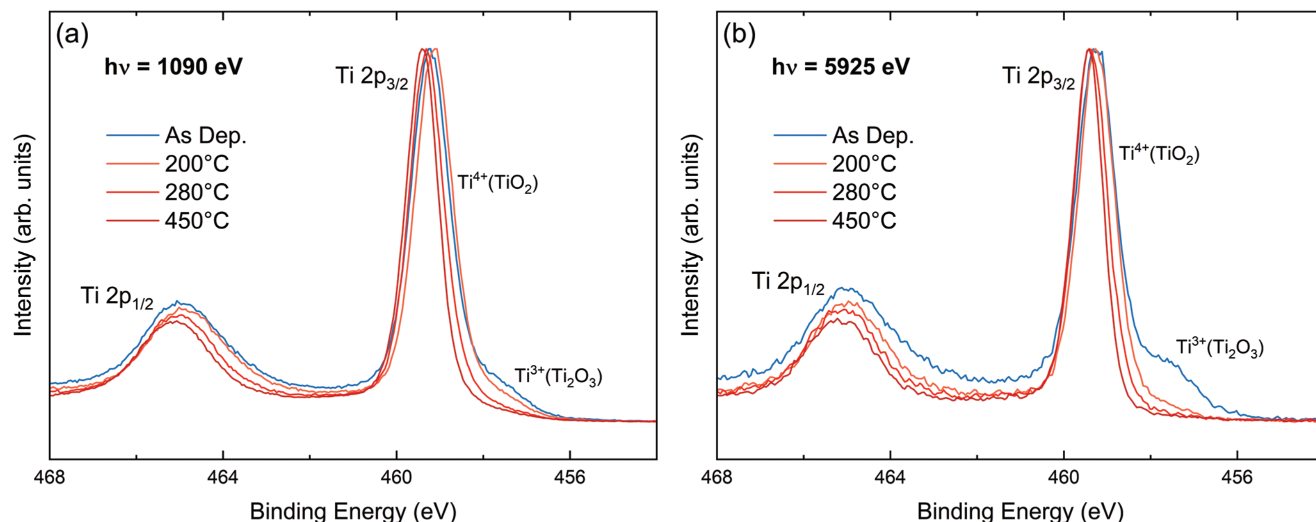

Figure 6. a) XPS and b) HAXPES Ti 2p core level photoemission spectra for titanium oxide films as deposited on SnO_2:F, and with 200, 280, and 450 °C post-deposition air anneals. Spectra have been normalized to the Ti^{4+}(TiO_2) $2p_{3/2}$ peak.

it was observed that the post-anneal in this case did not fully remedy the as-deposited oxygen deficiency, as shown by the optical transmission results in Figure S12 (Supporting Information). Raman spectra of these films show anatase at low temperatures, with mixed anatase-rutile phase observed at 200 °C and entirely rutile phase at 300 °C (Figure S13, Supporting Information). Thus, it would appear that the crystallization that occurs as a result of the high substrate temperature during deposition is deleterious in the case of polymorphic TiO_2 due to the effect of unwanted mixed-phase formation and suboxide Ti_2O_3 which is "locked-in" during deposition. Similar unwanted grain formation before the high-temperature anneal in solution spin-coated films may also act to impede final state crystalline quality.

In many cases, ETL characterization is either omitted from studies entirely, or substitute thicker films are deposited on alternative substrates (e.g., Si) to boost the diffraction signal. Another reason for substrate substitution is to simplify optical measurement for bandgap determination via the Tauc method,[77] although that presents its own limitations.[47] Clearly, this reduces the device relevance as the growth substrate and film thickness play crucial roles in material characteristics. The reasoning often given is that the films are simply too thin for characterization. While this may be true in some cases (resource and measurement dependent), clearly poor crystallinity in the acquired films is another deciding factor.[32] This effect of substrate dependant phase formation dynamics is highlighted in Figure S14

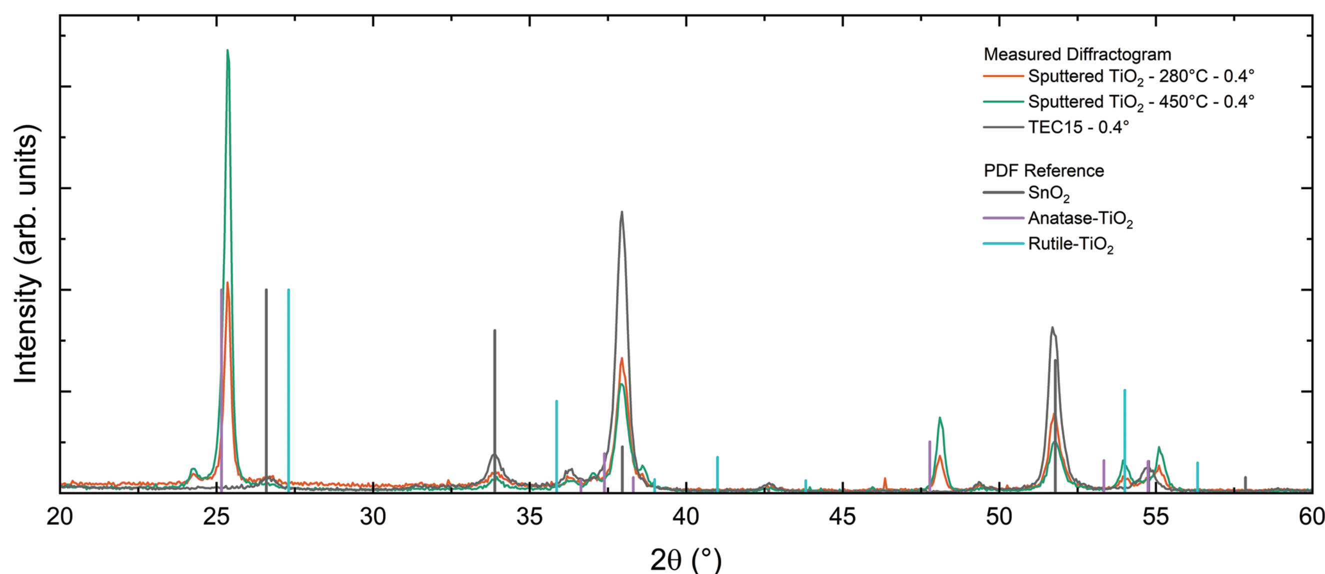

Figure 7. GIXRD for reactively sputtered titanium oxide films annealed at 280 and 450 °C, along with a SnO_2:F TEC15 substrate diffractogram for reference. Incident X-ray angle fixed at 0.4°. Also included are powder diffraction file (PDF) cards 9007433, 9008216, and 9004143 for SnO_2, anatase-TiO_2, and rutile-TiO_2, respectively.[72–75]

© 2024 The Author(s). Advanced Energy Materials published by Wiley-VCH GmbH

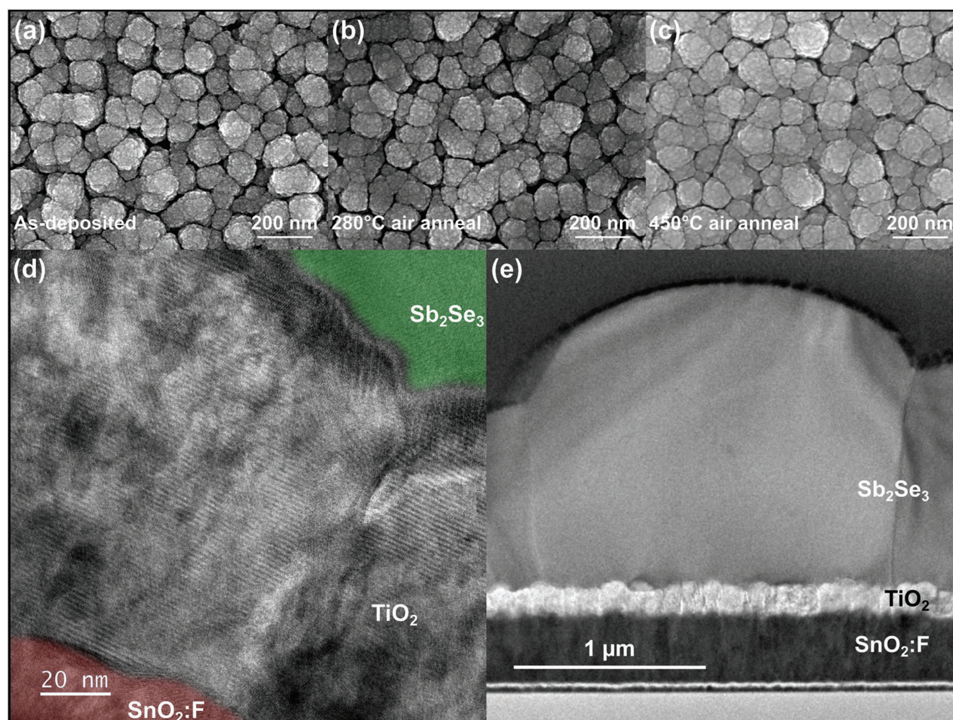

Figure 8. SEM of reactively sputtered titanium oxide films a) as-deposited and both b) 280 °C and c) 450 °C post-deposition air annealed. d) HRTEM of TiO_2 ETL cross-section from the completed device. e) Bright field TEM of SnO_2:F/TiO_2/Sb_2Se_3 cross-section.

(Supporting Information), where a witness Si substrate sample shared the same TiO_2 deposition run as an SnO_2:F substrate, but resulted in anatase and rutile phase TiO_2 films in the respective cases. Measurement of carrier concentration and mobility via the Hall effect, for example, becomes problematic in this respect, due to the requirement for film deposition onto non-conductive substrates. Interestingly, a Sb_2Se_3 device fabricated with the rutile-TiO_2 ETL reached a respectable 6.79% η (Figure S15, Supporting Information), demonstrating that anatase is not the only TiO_2 polymorph that can function as a high-performance ETL.

2.4. Champion Sb_2Se_3 Device

To properly assess the capability of Sb_2Se_3 heterojunction solar cell devices with the highly anatase reactively sputtered TiO_2 films, additional devices were fabricated with more optimized Sb_2Se_3 films. Literature regarding performance of Sb_2Se_3 solar cells largely focuses on optimization of the absorber layer itself, with grain structure, nanoribbon orientation, Sb/Se ratio and implementation of interfacial layers all reported as viable methods to achieve this.[8,27,43,78–84] In our own experience of growing Sb_2Se_3 on TiO_2, pinholes, interfacial voiding and formation of Sb_2O_3 phases have been the biggest challenges for achieving high-quality absorber material.[26,32,85]

Details of Sb_2Se_3 CSS growth conditions for initial devices from Figures 3 and 4 can be found in the Experimental Section. Whilst CSS conditions are equivalent within each device series, reactor evolution has meant that optimal conditions can drift over time and thus require periodic reoptimization. **Figure 9**a,b shows the champion Sb_2Se_3 cell with a 120 nm TiO_2 ETL reactively sputtered at RT with 5 W cm^{-2} power and 7.5% O_2 flow rate, post-annealed in air at 450 °C for 60 min. The Sb_2Se_3 film was grown with a two-step CSS process.[32,86] An initial seed layer was deposited with T_{source} = 460 °C, $T_{substrate}$ = 410 °C at vacuum for 15 min. The subsequent growth step was carried out at T_{source} = 530 °C and $T_{substrate}$ = 480 °C at 10 Torr for 10 min. The sample was then rapidly cooled under an N_2 atmosphere at 350 Torr. The resulting film again shows no diffraction signal from flat-lying hk0-oriented ribbons (Figure S16, Supporting Information).

The *J*–*V* scan in Figure 9a shows the device's resistance to shunting pathways in reverse bias that results from the pinhole blocking organic P3HT HTL, which is well established.[86,87] We have demonstrated through previous work[32] and optimization of the TiO_2 films in this present study (Figures 3 and 4) that device R_s is strongly dependent on the nature of TiO_2 ETL. The much reduced R_s of the cell in Figure 9a of 2.73 Ω cm^2 (taken at open-circuit) offers promise that cadmium-free Sb_2Se_3 devices can retain high *FF*, in addition to the inherent current extraction benefit from a wide bandgap ETL. Some light/dark crossover still persists in forward bias, indicative of either remaining interfacial charge barriers or photoconductivity effects.[37,88] Whilst there is no significant transformation of the EQE yield under illumination which was observed previously as a result of sputtered-TiO_2 films,[32] there remains a noticeable increase in sub-absorber-bandgap collection in the Urbach tail region >1030 nm (Figure 9b). This is surely related to the large V_{oc}-deficit in Sb_2Se_3 photovoltaics, which must be addressed through absorber defect control and doping approaches, largely not yet explored for this newly developing technology.[13]

© 2024 The Author(s). Advanced Energy Materials published by Wiley-VCH GmbH

16146840, 0, Downloaded from https://onlinelibrary.wiley.com/doi/10.1002/aenm.202401077 by Test, Wiley Online Library on [18/06/2024]. See the Terms and Conditions (https://onlinelibrary.wiley.com/terms-and-conditions) on Wiley Online Library for rules of use; OA articles are governed by the applicable Creative Commons License

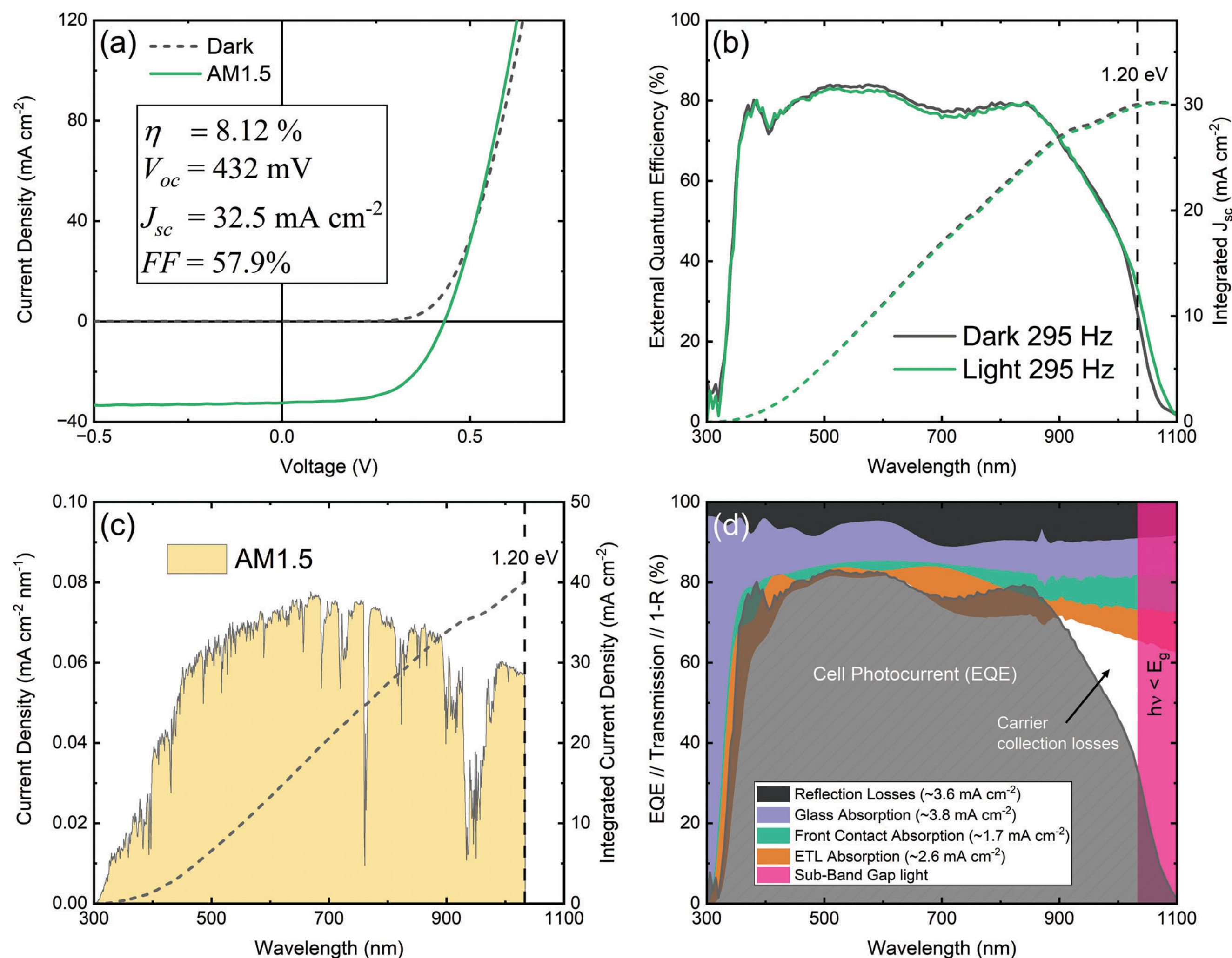

Figure 9. a) *J*–*V* and b) EQE of champion SnO_2:F/TiO_2/Sb_2Se_3/P3HT/Au cell. c) Maximum attainable current from AM1.5 for an Sb_2Se_3 device. d) Quantification of optical losses in a Glass/SnO_2:F/TiO_2/Sb_2Se_3/P3HT/Au device.

The 32.5 mA cm^{-2} J_{sc} (Figure 9a) is approaching the maximum obtainable after accounting for reflection and absorption losses in the 3.2 mm thick soda-lime glass TEC15 substrate (Figure 9c,d). The remaining carrier collection loss is entirely in the infrared region. We anticipate this is primarily due to recombination losses in the 1.2 µm-thick absorber, which is ≈5× thicker than is employed in the record Sb_2Se_3 device.[8] Approximate losses for each layer in the stack are provided, although optical interference effects with each subsequent layer results in a discrepancy between the EQE and spectrophotometry without applying the transfer-matrix method.[89] The dependence of TiO_2 thickness on optical interference of the full device stack is highlighted in Figure S17 (Supporting Information).

The significant improvement in the *FF* achieved here, compared to our prior work, and the demonstration of such a strong dependence of TiO_2 ETL film processing on the *FF* of subsequent Sb_2Se_3 photovoltaic devices, suggests that further optimization of ETLs themselves are effective routes to overcoming current device performance limits. There is, however, still some distance between the *FF* of the best CdS/Sb_2Se_3 devices (≈70%) and TiO_2/Sb_2Se_3 (≈60%). This *FF* disparity must be addressed by identifying the source of this sensitivity to interfacial charge accumulation and subsequently correcting charge dynamics at the electron selective contacts.

2.5. Device Simulations

The distinction between cliff-like and spike-like *CBO*s at an ETL/absorber interface was discussed in Section 1. Cliff-like offsets induce V_{oc}-loss via interfacial recombination and so spike-like offsets are preferred, although for large spikes, *J*–*V* distortion induces *FF* loss.[36–38] There is a general consensus within PV research that ≈0.4 eV is the limit before which distortion is induced.[37,39,46,90,91] This limit is of course system-dependent, with both the ETL and absorber properties defining the electrochemical interface. In the study by Kanevce and Sites et al.[39] on the CdS/CIS interface, it was demonstrated that the key value governing this distortion was the difference between the electron quasi-Fermi level and the *CBM* at the interface. They

© 2024 The Author(s). Advanced Energy Materials published by Wiley-VCH GmbH
16146840, 0, Downloaded from https://onlinelibrary.wiley.com/doi/10.1002/aenm.202401077 by Test, Wiley Online Library on [18/06/2024]. See the Terms and Conditions (https://onlinelibrary.wiley.com/terms-and-conditions) on Wiley Online Library for rules of use; OA articles are governed by the applicable Creative Commons License

16146840, 0, Downloaded from https://onlinelibrary.wiley.com/doi/10.1002/aenm.202401077 by Test, Wiley Online Library on [18/06/2024]. See the Terms and Conditions (https://onlinelibrary.wiley.com/terms-and-conditions) on Wiley Online Library for rules of use; OA articles are governed by the applicable Creative Commons License

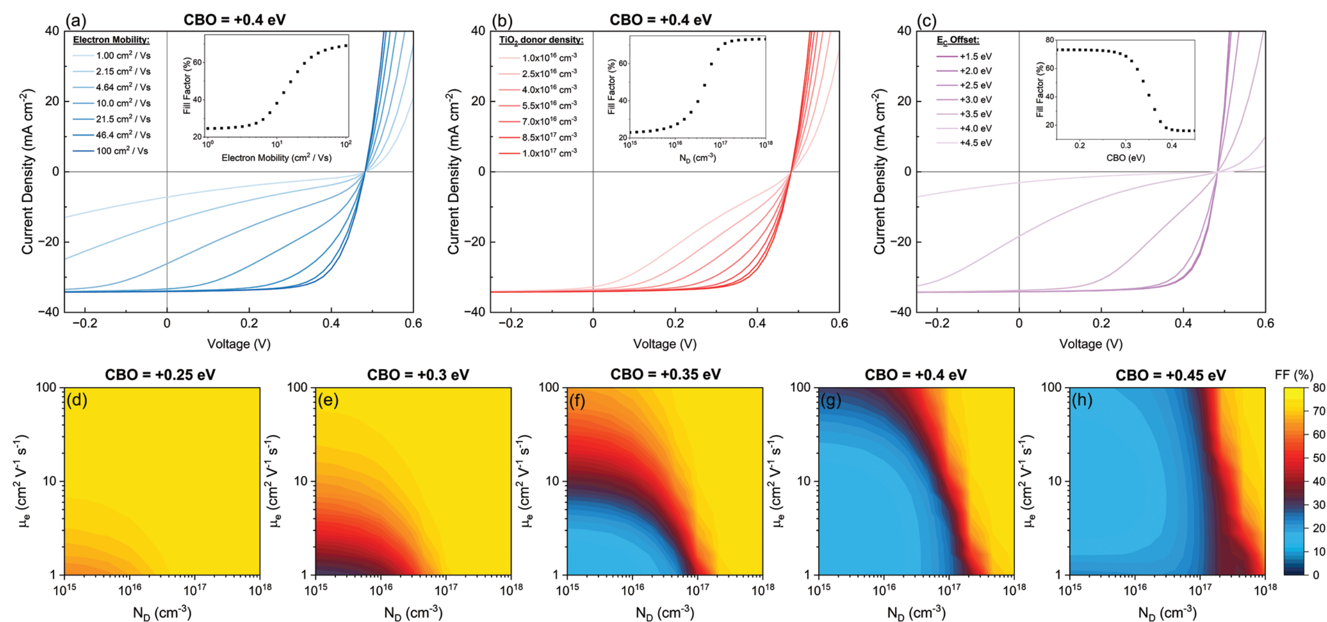

Figure 10. SCAPS-1D simulated current density–voltage measurements of Sb_2Se_3 devices with TiO_2 ETLs of varying a) electron mobility (μ_e), b) shallow donor density (N_D), c) conduction band offset (*CBO*) with corresponding *FF* inset. d–h) Contour plots showing *FF* dependency on both the TiO_2 μ_e and N_D for increasing *CBO*.

demonstrated that this value is influenced by the bulk *CBO*, shallow dopant density (N_D), acceptor trap density (N_{At}) and ETL thickness. Given the variable *J–V* distortion observed in the present study, our previous work, and seemingly elsewhere in Sb_2Se_3 literature with TiO_2 ETLs, a model of our device was constructed to allow for interrogation of the underlying device physics. The baseline Sb_2Se_3 device model is adapted from Medaille et al.,[92] which was defined using experimental data, and is detailed in Tables S4– S6 (Supporting Information).

In the baseline device structure, χ_e is set to –3.67 eV for anatase-TiO_2 and –4.08 for Sb_2Se_3 (*CBO* = 0.41 eV), as reported previously.[32] **Figure 10a,b** shows simulated *J–V* curves for devices with increasing μ_e and N_D of the TiO_2, respectively, at a fixed *CBO*. Literature reported values for room temperature μ_e of anatase-TiO_2 vary with crystallinity between 17 cm^2 V^{-1} s^{-1} for large single-crystals to 0.1 cm^2 V^{-1} s^{-1} for 20 nm nanoparticles.[93–96] As for carrier concentration, values vary between 10^{16} and 10^{19} cm^{-3},[97] primarily dependant on bulk V_O formation.[71]

In Figure 10a, it is demonstrated that for a fixed $1{\times}10^{17}$ cm^{-3} N_D, there is a strong dependence of μ_e on the device *FF*. Similarly, even with a sufficiently high μ_e (100 cm^2 V^{-1} s^{-1}), *J–V* distortion is induced by lowering N_D just one order of magnitude (Figure 10b). For completeness, *J–V* curves with increasing *CBO* for a fixed conductivity are simulated in Figure 10c and show a sharp *FF* reduction, as expected, beginning at +0.3 eV *CBO* (inset Figure 10c) for the chosen conductivity. The co-dependencies of μ_e and N_D on device *FF* are shown in the contour plots of Figure 10d–h for increasing bulk *CBO* values. The simulations reveal an abrupt loss in *FF* within a small range of reasonable TiO_2 electronic properties. These results suggest a TiO_2/Sb_2Se_3 *CBO* spike between +0.30 and +0.45 eV exists, but which experimentally can be mediated by sufficiently high conductivity of the TiO_2 layer.

In addition to the TiO_2 bulk electronic properties investigated in Figure 10, the effects of interface states were also explored. Reduction of the TiO_2 surface is known to produce a mid-gap feature with Ti 3d character in photoemission of both anatase and rutile, which appears ≈2 eV above the *VBM*.[98,99] This is observed experimentally in TiO_2 films fabricated via solution spin-coating and RF sputtered from a compound TiO_2 target; however this defect peak appears absent in the TiO_2 films synthesized from the DC reactive sputtering method as shown in Figure S18 (Supporting Information). Hence it seems reasonable to enquire whether this defect state influences the *J–V* distortion. The effects of incorporating this acceptor-type interfacial defect 2.2 eV above the TiO_2 *VBM* are explored in **Figure 11**.

It is evident that for high interfacial defect densities, *J–V* distortion can be induced even for the case where the ETL/absorber *CBM*s are nearly aligned (*CBO* = +0.05 eV), due to Fermi-level pinning, as discussed by Klenk.[36] However, in this scenario, a high interfacial defect density increases V_{oc}, and is more apparent for smaller *CBO*s. Presumably, this is linked to the relative energy position of the hole quasi-Fermi level in the Sb_2Se_3 to the acceptor-type TiO_2 surface defect which will decrease as the TiO_2 χ_e is decreased in order to investigate the *CBO*. Experimentally, this is not observed as V_{oc} appears largely independent of *J–V* distortion (Figure 4).[32]

Modulation of charge states in such acceptor-type defects with illumination is further suggested experimentally by photoconductive effects, namely; crossover in the light and dark *J–V* curve presented here (Figure 9a),[37] and anomalous light-biased EQE measurements exceeding unity, dependant on chopping frequency.[32] This is perhaps further evidence of a spike-like

© 2024 The Author(s). Advanced Energy Materials published by Wiley-VCH GmbH

16146840, 0, Downloaded from https://onlinelibrary.wiley.com/doi/10.1002/aenm.202401077 by Test, Wiley Online Library on [18/06/2024]. See the Terms and Conditions (https://onlinelibrary.wiley.com/terms-and-conditions) on Wiley Online Library for rules of use; OA articles are governed by the applicable Creative Commons License

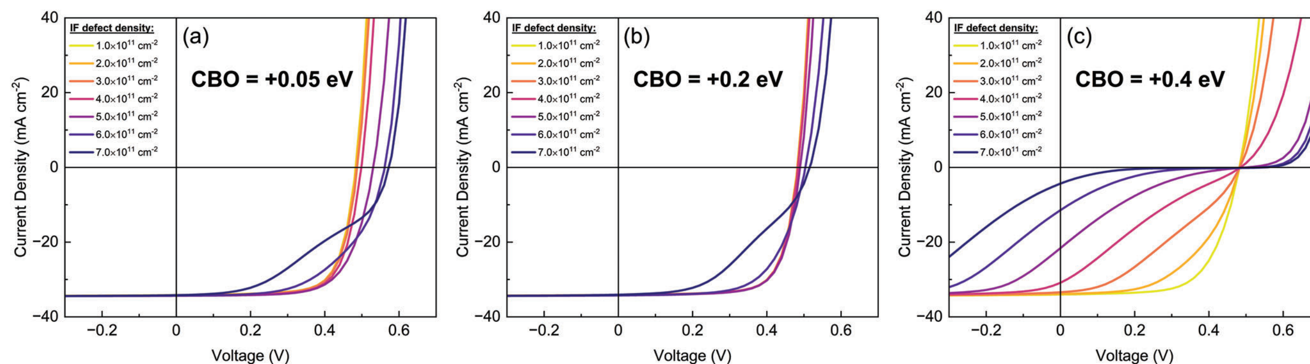

Figure 11. SCAPS-1D simulated current density–voltage measurements of Sb_2Se_3 devices with TiO_2 ETLs of varying interfacial defect density for a) +0.05 eV, b) +0.2 eV, and c) +0.4 eV *CBO*, which is located 2.2 eV above the TiO_2 *VBM*.

CBO where the V_{oc} is invariable and the inflection point of the distortion is fixed at open-circuit, unlike in Figure 11a,b.

Variability in previous work and performance dependence on thickness can be explained by TiO_2 sensitivity to processing conditions and crystallite size, which are well-established.[71,93,97] The device modeling simulations support evidence from select natural band alignment measurements that a spike-like *CBO* exists between anatase-TiO_2 and Sb_2Se_3,[32] although reported band positions are highly variable as discussed in Section 1. Fundamentally the respective band positions should be largely fixed, and variance in device behavior is more likely regulated by electronic properties. Thus, fabrication of highly crystalline TiO_2 for enhanced μ_e and reduced surface defect density, alongside increased carrier concentration through oxygen-deficient processing, is surely favorable to navigate the *CBO* of these materials.

The *FF* of TiO_2/Sb_2Se_3 devices may inherently be limited by such a *CBO* spike, but TiO_2 doping approaches are yet to be explored. Alloyed $Sb_2(S,Se)_3$ absorbers may offer *CBO* tunability and Liu et al. have already made progress in this direction, demonstrating an R_s reduction by increasing the sulfur content (and thus bandgap) in the near-interface region.[63] For pure Sb_2Se_3 devices, alternative metal oxide ETLs may need to be explored, if the *CBO* induced by the TiO_2 interface cannot be alleviated by alternative means.

3. Conclusion

In summary, we have investigated the relationship between TiO_2 thin-film fabrication conditions and the performance of subsequent Sb_2Se_3 photovoltaic devices with TiO_2 acting as an ETL. The method proposed here of reactive DC sputtering from a metallic Ti target offers a high throughput, scalable method of producing high-quality compound TiO_2 thin films for this photovoltaic application. Through spectrophotometry, SEM, XRD, photoemission and Raman spectroscopy characterization, the development of the reactively sputtered TiO_2 thin-films during the post-deposition anneal process has been studied and compared with conventional spin-coated films from a TTIP precursor solution. Improved crystallinity of anatase-TiO_2 is observed in reactively sputtered films, driving a reduction in R_s which has historically been a key performance limiting factor for Sb_2Se_3 devices of this architecture. This reduction in R_s and subsequent improvement in *FF* ultimately delivers the highest efficiency cadmium-free Sb_2Se_3 photovoltaic device reported to date.

The effects of varying the μ_e, N_D and surface acceptor-type defect density of TiO_2 on device performance are investigated through device modeling simulations which infer the presence of a spike-like *CBO* between Sb_2Se_3 and TiO_2. The result provides a robust explanation for *FF* variability in Sb_2Se_3 devices fabricated with TiO_2 ETLs, and highlights the ETL parameters most critical for developing high-performance cadmium-free devices.

Whilst this step forward only goes some of the way to bridging the gap between state-of-the-art CdS and at-present unconventional wide bandgap metal oxide ETL devices, this result can act as an incentive for an accelerated transition away from CdS ETLs, which surely must happen for the long-term commercialization of Sb_2Se_3 solar cells.

4. Experimental Section

Device Fabrication: All devices fabricated for this study comprised a superstrate-oriented SnO_2:F/TiO_2/Sb_2Se_3/P3HT/Au architecture. TEC15 glass (3.2 mm-thick) from Greatcell Solar Materials was used as the soda–lime glass substrate and transparent conductive oxide front contact. The TEC15 substrate was cleaned using isopropyl alcohol, 2% Hellmanex in a deionized water solution and a further 15 min UV ozone treatment. The DC magnetron reactively sputtered TiO_2 films were sputtered from a 76 mm diameter Ti target (4N purity, PI-KEM) in 5 mTorr pressure at 5 W cm^{-2} power density. The combined O_2+Ar gas flow rate during sputter deposition was 20 sccm for all films. Oxygen concentration is defined as the percentage of O_2 flow contributed to total 20 sccm. Spin-coated TiO_2 films were deposited from a 0.3 M concentration of TTIP in an ethyl alcohol solution. Two 275 µL doses of the solution were sequentially spin-cast at 3000 rpm in a N_2 atmosphere, with a 10 min 120 °C hot plate anneal after each dose to drive off the remaining solvent. The HiPIMS TiO_2 films were fabricated by High Power Impulse Magnetron Sputtering in a Lesker CMS-18 deposition system by reactive magnetron sputtering from a Ti target (4N purity) with 100 mm diameter. The HiPIMS process was operated with an average power of 500 W, corresponding to 6.4 W cm^{-2}. The pulse on time was set to 100 µs and the frequency to 1 kHz. The depositions were carried out in poisoned (oxide) mode with 60 sccm Ar and 6 sccm O_2, at a pressure of 6 mTorr. Unless otherwise stated, as-deposited TiO_2 films were post-annealed in air at 450 °C for 60 min. Prior to Sb_2Se_3 deposition, the TiO_2 films were ozone-cleaned for 15 min. Alfa Aesar 5N granulate Sb_2Se_3 source material was deposited on to the TiO_2 surface via a two-step CSS process. An initial 15 min seed layer was deposited at a vacuum with respective source and substrate temperatures of 440–450 and 400–410 °C. A subsequent 10 min growth step at 10 Torr N_2 with respective source

© 2024 The Author(s). Advanced Energy Materials published by Wiley-VCH GmbH

and substrate temperatures of 530 and 480–490 °C followed to deliver a 1.2 µm-thick film. The HTL was deposited from a 10 mg mL^{-1} solution of P3HT in chlorobenzene by spin-casting 75 µL at 3000 rpm. 0.1 cm^2 50 nm thick gold back contacts were then thermally evaporated onto the P3HT surface.

Material Characterization: Film thicknesses were measured using a cntech AMBIOS XP-200 stylus profilometer. *J–V* measurements were taken using a TS Space Systems solar simulator (class AAA) calibrated to AM1.5G. EQE measurements were taken with a Bentham PVE300 system. Quartz-halogen white light-biased EQE was calibrated to a power density of 100 mW cm^{-2}. Transmission and reflectivity measurements were taken using a Shimadzu SolidSpec-3700 UV–vis spectrophotometer. Raman spectra were obtained from a Renishaw InVia system operated with a 532 nm laser with 5 s acquisitions at 10 mW for 15 accumulations. The system was calibrated to the 520 cm^{-1} peak from a Si wafer, with a resolution of 1 cm^{-1}. Photoemission measurements were carried out at the I09 beamline of the Diamond Light Source facility for photon energies of 1090 and 5925 eV. Two-point energy calibration was performed by measuring the Fermi edge and Au 4f$_{7/2}$ core-level peak position of a 200 nm Au film at both hard and soft photon energies. A 50 meV step size was used for all core levels with 200 and 70 meV pass energy for hard and soft photon energies, respectively. θ-2θ XRD measurements were obtained from a Rigaku SmartLab diffractomator with a Cu anode (λ = 1.542 Å) and a Ge(220) monochromator in parallel beam configuration. Grazing incidence (GIXRD) geometry was used to reduce the intensity from the underlying substrate and selectively probe the TiO_2 layer. This was performed at an incident angle of $\Omega = 0.4°$ and $\Omega = 0.6°$, with a 5° incident slit and 0.114° parallel slit analyzer using non-monochromated Cu K$\alpha_{1,2}$ X-rays. Scanning Electron microscopy was carried out on a Zeiss Sigma 300vp electron microscope operated at 5 keV in Secondary Electron InLens imaging. TEM micrographs were obtained using a JEOL 2100F Transmission Electron Microscope equipped with an Oxford Instrument X-Max 65, operated by 200 keV. The TEM lamella was prepared using an FEI Helios Nano lab 600 MK2.

Supporting Information

Supporting Information is available from the Wiley Online Library or from the author.

Acknowledgements

Funding for the work was provided by the EPSRC via EP/T006188/1 and EP/W03445X/1. Diamond Light Source is acknowledged for I09 beam time under proposal SI34642-1. Data files related to the project are available from DOI: 10.5281/zenodo.11220485 or from the corresponding author. The baseline TiO_2/Sb_2Se_3 SCAPS-1D device model is available online.

Conflict of Interest

The authors declare no conflict of interest.

Data Availability Statement

The data that support the findings of this study are openly available in Reactive DC Sputtered TiO_2 Electron Transport Layers for Cadmium-Free Sb_2Se_3 Solar Cells at 10.5281/zenodo.11220485, reference number 11220485.

Keywords

antimony, photovoltaics, Sb_2Se_3, selenide, sputtering, solar, TiO_2

Received: March 8, 2024
Revised: May 20, 2024
Published online:

[1] M. A. Green, E. D. Dunlop, M. Yoshita, N. Kopidakis, K. Bothe, G. Siefer, X. Hao, *Prog. Photovoltaics* **2023**, *31*, 651.
[2] G. Fevola, P. S. Jørgensen, M. Verezhak, A. Slyamov, A. Crovetto, Z. I. Balogh, C. Rein, S. Canulescu, J. W. Andreasen, *Phys. Rev. Res.* **2020**, *2*, 013378.
[3] M. Birkett, W. M. Linhart, J. Stoner, L. J. Phillips, K. Durose, J. Alaria, J. D. Major, R. Kudrawiec, T. D. Veal, *APL Mater.* **2018**, *6*, 084901.
[4] M. Y. Versavel, J. A. Haber, *Thin Solid Films* **2007**, *515*, 7171.
[5] X. Wang, R. Tang, C. Wu, C. Zhu, T. Chen, *J. Energy Chem.* **2018**, *27*, 713.
[6] R. Tang, Z.-H. Zheng, Z.-H. Su, X.-J. Li, Y.-D. Wei, X.-H. Zhang, Y.-Q. Fu, J.-T. Luo, P. Fan, G.-X. Liang, *Nano Energy* **2019**, *64*, 103929.
[7] N. Fleck, O. S. Hutter, L. J. Phillips, H. Shiel, T. D. C. Hobson, V. R. Dhanak, T. D. Veal, F. Jäckel, K. Durose, J. D. Major, *ACS Appl. Mater. Interfaces* **2020**, *12*, 52595.
[8] Y. Zhao, S. Wang, C. Li, B. Che, X. Chen, H. Chen, R. Tang, X. Wang, G. Chen, T. Wang, J. Gong, T. Chen, X. Xiao, J. Li, *Energy Environ. Sci.* **2022**, *15*, 5118.
[9] X. Chen, B. Che, Y. Zhao, S. Wang, H. Li, J. Gong, G. Chen, T. Chen, X. Xiao, J. Li, *Adv. Energy Mater.* **2023**, *13*, 2300391.
[10] S. Resalati, T. Okoroafor, A. Maalouf, E. Saucedo, M. Placidi, *Appl. Energy* **2022**, *313*, 118888.
[11] J. Kephart, J. McCamy, Z. Ma, A. Ganjoo, F. Alamgir, W. Sampath, *Sol. Energy Mater. Sol. Cells* **2016**, *157*, 266.
[12] M. A. Scarpulla, B. McCandless, A. B. Phillips, Y. Yan, M. J. Heben, C. Wolden, G. Xiong, W. K. Metzger, D. Mao, D. Krasikov, I. Sankin, S. Grover, A. Munshi, W. Sampath, J. R. Sites, A. Bothwell, D. Albin, M. O. Reese, A. Romeo, M. Nardone, R. Klie, J. M. Walls, T. Fiducia, A. Abbas, S. M. Hayes, *Sol. Energy Mater. Sol. Cells* **2023**, *255*, 112289.
[13] C. H. Don, T. P. Shalvey, J. D. Major, *PRX Energy* **2023**, *2*, 041001.
[14] J. R. Sites, *Sol. Energy Mater. Sol. Cells* **2003**, *75*, 243.
[15] J. M. Kephart, R. Geisthardt, W. Sampath, in *2012 38th IEEE Photovoltaic Specialists Conference*, IEEE, Austin, TX, USA, **2012**, pp. 000854–000858.
[16] J. M. Kephart, R. M. Geisthardt, W. S. Sampath, *Prog. Photovoltaics* **2015**, *23*, 1484.
[17] Y. Itzhaik, O. Niitsoo, M. Page, G. Hodes, *J. Phys. Chem. C* **2009**, *113*, 4254.
[18] Y. Zhou, M. Leng, Z. Xia, J. Zhong, H. Song, X. Liu, B. Yang, J. Zhang, J. Chen, K. Zhou, J. Han, Y. Cheng, J. Tang, *Adv. Energy Mater.* **2014**, *4*, 1301846.
[19] Y. C. Choi, T. N. Mandal, W. S. Yang, Y. H. Lee, S. H. Im, J. H. Noh, S. I. Seok, *Angew. Chem., Int. Ed.* **2014**, *53*, 1329.
[20] Y. C. Choi, D. U. Lee, J. H. Noh, E. K. Kim, S. I. Seok, *Adv. Funct. Mater.* **2014**, *24*, 3587.
[21] M. Leng, M. Luo, C. Chen, S. Qin, J. Chen, J. Zhong, J. Tang, *Appl. Phys. Lett.* **2014**, *105*, 083905.
[22] G.-X. Liang, Y.-D. Luo, S. Chen, R. Tang, Z.-H. Zheng, X.-J. Li, X.-S. Liu, Y.-K. Liu, Y.-F. Li, X.-Y. Chen, Z.-H. Su, X.-H. Zhang, H.-L. Ma, P. Fan, *Nano Energy* **2020**, *73*, 104806.
[23] G. Liang, M. Chen, M. Ishaq, X. Li, R. Tang, Z. Zheng, Z. Su, P. Fan, X. Zhang, S. Chen, *Adv. Sci.* **2022**, *9*, 2105142.
[24] R. Tang, S. Chen, Z.-H. Zheng, Z.-H. Su, J.-T. Luo, P. Fan, X.-H. Zhang, J. Tang, G.-X. Liang, *Adv. Mater.* **2022**, *34*, 2109078.
[25] S. Dong, G. Li, J. Hong, R. Qi, S. Yang, P. Yang, L. Sun, F. Yue, *Phys. Chem. Chem. Phys.* **2023**, *25*, 4617.
[26] L. J. Phillips, C. N. Savory, O. S. Hutter, P. J. Yates, H. Shiel, S. Mariotti, L. Bowen, M. Birkett, K. Durose, D. O. Scanlon, J. D. Major, *IEEE J. Photovoltaics* **2019**, *9*, 544.
[27] Z. Li, X. Liang, G. Li, H. Liu, H. Zhang, J. Guo, J. Chen, K. Shen, X. San, W. Yu, R. E. Schropp, Y. Mai, *Nat. Commun.* **2019**, *10*, 1.
[28] R. E. Williams, Q. M. Ramasse, K. P. McKenna, L. J. Phillips, P. J. Yates, O. S. Hutter, K. Durose, J. D. Major, B. G. Mendis, *ACS Appl. Mater. Interfaces* **2020**, *12*, 21730.

© 2024 The Author(s). Advanced Energy Materials published by Wiley-VCH GmbH

16146840, 0, Downloaded from https://onlinelibrary.wiley.com/doi/10.1002/aenm.202401077 by Test, Wiley Online Library on [18/06/2024]. See the Terms and Conditions (https://onlinelibrary.wiley.com/terms-and-conditions) on Wiley Online Library for rules of use; OA articles are governed by the applicable Creative Commons License

16146840, 0, Downloaded from https://onlinelibrary.wiley.com/doi/10.1002/aenm.202401077 by Test, Wiley Online Library on [18/06/2024]. See the Terms and Conditions (https://onlinelibrary.wiley.com/terms-and-conditions) on Wiley Online Library for rules of use; OA articles are governed by the applicable Creative Commons License

[29] S. Lu, H. Ding, J. Hu, Y. Liu, J. Zhu, R. Kondrotas, C. Chen, J. Tang, *Appl. Phys. Lett.* **2020**, *116*, 241602.
[30] C. Chen, Y. Zhao, S. Lu, K. Li, Y. Li, B. Yang, W. Chen, L. Wang, D. Li, H. Deng, F. Yi, J. Tang, *Adv. Energy Mater.* **2017**, *7*, 1700866.
[31] M. Koltsov, R. Krautmann, A. Katerski, N. Maticiuc, M. Krunks, I. Oja Acik, N. Spalatu, *Faraday Discuss.* **2022**, *239*, 273.
[32] C. H. Don, T. P. Shalvey, M. J. Smiles, L. Thomas, L. J. Phillips, T. D. C. Hobson, H. Finch, L. A. H. Jones, J. E. N. Swallow, N. Fleck, C. Markwell, P. K. Thakur, T.-L. Lee, D. Biswas, L. Bowen, B. A. D. Williamson, D. O. Scanlon, V. R. Dhanak, K. Durose, T. D. Veal, J. D. Major, *Adv. Mater. Interfaces* **2023**, *10*, 2300238.
[33] U. Würfel, A. Cuevas, P. Würfel, *IEEE J. Photovoltaics* **2015**, *5*, 461.
[34] U. Rau, T. Kirchartz, *Adv. Mater. Interfaces* **2019**, *6*, 1900252.
[35] A. Onno, C. Chen, P. Koswatta, M. Boccard, Z. C. Holman, *J. Appl. Phys.* **2019**, *126*, 183103.
[36] R. Klenk, *Thin Solid Films* **2001**, *387*, 135.
[37] M. Gloeckler, C. Jenkins, J. R. Sites, *MRS Proc.* **2003**, *763*, B5.20.
[38] M. Gloeckler, J. Sites, *Thin Solid Films* **2005**, *480-481*, 241.
[39] A. Kanevce, M. Gloeckler, A. O. Pudov, J. R. Sites, *MRS Online Proc. Libr.* **2005**, *865*, 532.
[40] R. Saive, *IEEE J. Photovoltaics* **2019**, *9*, 1477.
[41] H. Shiel, O. S. Hutter, L. J. Phillips, J. E. N. Swallow, L. A. H. Jones, T. J. Featherstone, M. J. Smiles, P. K. Thakur, T.-L. Lee, V. R. Dhanak, J. D. Major, T. D. Veal, *ACS Appl. Energy Mater.* **2020**, *3*, 11617.
[42] W. Wang, Z. Cao, H. Wang, J. Luo, Y. Zhang, *J. Mater. Chem. A* **2021**, *9*, 26963.
[43] Y. Wang, R. Tang, L. Huang, C. Qian, W. Lian, C. Zhu, T. Chen, *ACS Appl. Mater. Interfaces* **2022**, *14*, 33181.
[44] W. Wang, L. Yao, J. Dong, L. Wu, Z. Cao, L. Hui, G. Chen, J. Luo, Y. Zhang, *Adv. Mater. Interfaces* **2022**, *9*, 2102464.
[45] J. Han, X. Pu, H. Zhou, Q. Cao, S. Wang, Z. He, B. Gao, T. Li, J. Zhao, X. Li, *ACS Appl. Mater. Interfaces* **2020**, *12*, 44297.
[46] G. Teeter, S. P. Harvey, C. L. Perkins, K. Ramanathan, I. L. Repins, *J Vac Sci Technol, A* **2019**, *37*, 031202.
[47] J. Klein, L. Kampermann, B. Mockenhaupt, M. Behrens, J. Strunk, G. Bacher, *Adv. Funct. Mater.* **2023**, *33*, 2304523.
[48] D. Depla, S. Mahieu, *Reactive Sputter Deposition*, Springer Berlin, Heidelberg **2008**.
[49] T. Kubart, D. Depla, D. M. Martin, T. Nyberg, S. Berg, *Appl. Phys. Lett.* **2008**, *92*, 221501.
[50] S. Berg, T. Nyberg, *Thin Solid Films* **2005**, *476*, 215.
[51] K. Strijckmans, R. Schelfhout, D. Depla, *J. Appl. Phys.* **2018**, *124*, 241101.
[52] S. Mariotti, O. S. Hutter, L. J. Phillips, P. J. Yates, B. Kundu, K. Durose, *ACS Appl. Mater. Interfaces* **2018**, *10*, 3750.
[53] Y. Hu, L. Huang, B. Che, H. Wang, A. Liu, C. Zhu, R. Tang, T. Chen, *Adv. Funct. Mater.* **2024**, *34*, 2314974.
[54] M. Liao, H. Niu, G. Chen, *Thin Solid Films* **2010**, *518*, 7258.
[55] D. F. Fernandes, L. Österlund, T. Kubart, *Surf. Coat. Technol.* **2023**, *467*, 129659.
[56] T. Kubart, O. Kappertz, T. Nyberg, S. Berg, *Thin Solid Films* **2006**, *515*, 421.
[57] A. Belaidi, R. Bayón, L. Dloczik, K. Ernst, M. Lux-Steiner, R. Könenkamp, *Thin Solid Films* **2003**, *431-432*, 488.
[58] T. Baines, K. Durose, J. D. Major, in *2018 IEEE 7th World Conference on Photovoltaic Energy Conversion (WCPEC) (A Joint Conference of 45th IEEE PVSC, 28th PVSEC & 34th EU PVSEC)*, **2018**, pp. 2974–2979.
[59] T. Baines, G. Zoppi, L. Bowen, T. P. Shalvey, S. Mariotti, K. Durose, J. D. Major, *Sol. Energy Mater. Sol. Cells* **2018**, *180*, 196.
[60] C. S. Ferekides, D. L. Morel, *Phase I Annual Technical Report October 2005 – September 2006*, **2011**.
[61] D.-B. Li, Z. Song, R. A. Awni, S. S. Bista, N. Shrestha, C. R. Grice, L. Chen, G. K. Liyanage, M. A. Razooqi, A. B. Phillips, M. J. Heben, R. J. Ellingson, Y. Yan, *ACS Appl. Energy Mater.* **2019**, *2*, 2896.
[62] T. P. Shalvey, H. Bagshaw, J. D. Major, *ACS Appl. Mater. Interfaces* **2022**, *14*, 42188.
[63] C. Liu, S. Wu, Y. Gao, Y. Feng, X. Wang, Y. Xie, J. Zheng, H. Zhu, Z. Li, R. E. Schropp, K. Shen, Y. Mai, *Adv. Funct. Mater.* **2022**, *32*, 2209601.
[64] D. A. H. Hanaor, C. C. Sorrell, *J. Mater. Sci.* **2011**, *46*, 855.
[65] J. Zhang, M. Li, Z. Feng, J. Chen, C. Li, *J. Phys. Chem. B* **2006**, *110*, 927.
[66] R. L. Kurtz, V. E. Henrich, *Surf. Sci. Spectra* **1998**, *5*, 179.
[67] M. C. Biesinger, L. W. Lau, A. R. Gerson, R. S. Smart, *Appl. Surf. Sci.* **2010**, *257*, 887.
[68] D. Koch, S. Manzhos, *J. Phys. Chem. Lett.* **2017**, *8*, 1593.
[69] A. Walsh, A. A. Sokol, J. Buckeridge, D. O. Scanlon, C. R. A. Catlow, *J. Phys. Chem. Lett.* **2017**, *8*, 2074.
[70] G. V. Samsonov, *The Oxide Handbook*, Springer New York, NY, **1982**.
[71] U. Diebold, *Surf. Sci. Rep.* **2003**, *48*, 53.
[72] W. H. Baur, *Acta Crystallogr.* **1956**, *9*, 515.
[73] M. Horn, C. F. Schwebdtfeger, E. P. Meagher, *Z. Kristallogr. Cryst. Mater.* **1972**, *136*, 273.
[74] E. P. Meagher, G. A. Lager, *Canad. Mineral.* **1979**, *17*, 77.
[75] R. E. Newnham, Y. M. de Haan, *Z. Kristallogr.* **1962**, *117*, 235.
[76] M. Birkholz, P. F. Fewster, C. Genzel, *Thin film analysis by X-ray scattering / Mario Birkholz with contributions by Paul F. Fewster, Christoph Genzel*, Wiley-VCH, Weinheim **2006**.
[77] J. Tauc, *Mater. Res. Bull.* **1968**, *3*, 37.
[78] Y. Zhou, L. Wang, S. Chen, S. Qin, X. Liu, J. Chen, D.-J. Xue, M. Luo, Y. Cao, Y. Cheng, E. H. Sargent, J. Tang, *Nat. Photonics* **2015**, *9*, 409.
[79] K. Li, C. Chen, S. Lu, C. Wang, S. Wang, Y. Lu, J. Tang, *Adv. Mater.* **2019**, *31*, 1903914.
[80] K. Shen, Y. Zhang, X. Wang, C. Ou, F. Guo, H. Zhu, C. Liu, Y. Gao, R. E. I. Schropp, Z. Li, X. Liu, Y. Mai, *Adv. Sci.* **2020**, *7*, 2001013.
[81] P. Fan, G.-J. Chen, S. Chen, Z.-H. Zheng, M. Azam, N. Ahmad, Z.-H. Su, G.-X. Liang, X.-H. Zhang, Z.-G. Chen, *ACS Appl. Mater. Interfaces* **2021**, *13*, 46671.
[82] Z. Duan, X. Liang, Y. Feng, H. Ma, B. Liang, Y. Wang, S. Luo, S. Wang, R. E. I. Schropp, Y. Mai, Z. Li, *Adv. Mater.* **2022**, *34*, 2202969.
[83] Y. Zhao, S. Wang, C. Jiang, C. Li, P. Xiao, R. Tang, J. Gong, G. Chen, T. Chen, J. Li, X. Xiao, *Adv. Energy Mater.* **2022**, *12*, 2103015.
[84] T. P. Weiss, I. Minguez-Bacho, E. Zuccalá, M. Melchiorre, N. Valle, B. El Adib, T. Yokosawa, E. Spiecker, J. Bachmann, P. J. Dale, S. Siebentritt, *Prog. Photovoltaics* **2023**, *31*, 203.
[85] D. A. Sindi, T. P. Shalvey, J. D. Major, *Mater. Sci. Semicond. Process.* **2024**, *174*, 108161.
[86] O. S. Hutter, L. J. Phillips, K. Durose, J. D. Major, *Sol. Energy Mater. Sol. Cells* **2018**, *188*, 177.
[87] J. Major, L. Phillips, M. A. Turkestani, L. Bowen, T. Whittles, V. Dhanak, K. Durose, *Sol. Energy Mater. Sol. Cells* **2017**, *172*, 1.
[88] R. Scheer, H.-W. Schock, *Chalcogenide Photovoltaics: Physics, Technologies, and Thin Film Devices*, Wiley-VCH, **2011**.
[89] J. M. Ball, S. D. Stranks, M. T. Hörantner, S. Hüttner, W. Zhang, E. J. W. Crossland, I. Ramirez, M. Riede, M. B. Johnston, R. H. Friend, H. J. Snaith, *Energy Environ. Sci.* **2015**, *8*, 602.
[90] X. Liu, J. R. Sites, *AIP Conf. Proc.* **1996**, *353*, 444.
[91] T. Minemoto, T. Matsui, H. Takakura, Y. Hamakawa, T. Negami, Y. Hashimoto, T. Uenoyama, M. Kitagawa, *Sol. Energy Mater. Sol. Cells* **2001**, *67*, 83.
[92] A. Gon Medaille, K. J. Tiwari, S. Giraldo, M. Placidi, E. Saucedo, Z. Jehl Li-Kao, *Solar RRL* **2022**, *6*, 2100911.
[93] Y. Mi, Y. Weng, *Sci. Rep.* **2015**, *5*, 11482.
[94] T. S. Krasienapibal, T. Fukumura, Y. Hirose, T. Hasegawa, *Jpn. J. Appl. Phys.* **2014**, *53*, 090305.
[95] L. Forro, O. Chauvet, D. Emin, L. Zuppiroli, H. Berger, F. Lévy, *J. Appl. Phys.* **1994**, *75*, 633.
[96] Y. Tamaki, K. Hara, R. Katoh, M. Tachiya, A. Furube, *J. Phys. Chem. C* **2009**, *113*, 11741.

© 2024 The Author(s). Advanced Energy Materials published by Wiley-VCH GmbH

[97] M. C. Sellers, E. G. Seebauer, *Thin Solid Films* **2011**, *519*, 2103.
[98] A. G. Thomas, W. R. Flavell, A. R. Kumarasinghe, A. K. Mallick, D. Tsoutsou, G. C. Smith, R. Stockbauer, S. Patel, M. Grätzel, R. Hengerer, *Phys. Rev. B* **2003**, *67*, 035110.
[99] A. G. Thomas, W. R. Flavell, A. K. Mallick, A. R. Kumarasinghe, D. Tsoutsou, N. Khan, C. Chatwin, S. Rayner, G. C. Smith, R. L. Stockbauer, S. Warren, T. K. Johal, S. Patel, D. Holland, A. Taleb, F. Wiame, *Phys. Rev. B* **2007**, *75*, 035105.

© 2024 The Author(s). Advanced Energy Materials published by Wiley-VCH GmbH

16146840, 0, Downloaded from https://onlinelibrary.wiley.com/doi/10.1002/aenm.202401077 by Test, Wiley Online Library on [18/06/2024]. See the Terms and Conditions (https://onlinelibrary.wiley.com/terms-and-conditions) on Wiley Online Library for rules of use; OA articles are governed by the applicable Creative Commons License